Research Article

Hot deformation of high-Nb-containing γ-TiAl alloy in the temperature range of 1000–1200 °C: microstructural attributes to hot workability

Vajinder Singh[1,2] · Atul Kumar[1] · Chandan Mondal[1] · P. P. Bhattacharjee[2] · P. Ghosal[1]

Abstract

Hot deformation behavior of a high-Nb-containing cast γ-TiAl-based Ti–45Al–8Nb (at.%) alloy has been investigated in the temperature range of 1000–1200 °C and the strain rate range of 0.5–0.005 s^{-1}. The alloy shows an initial microstructure of coarse lamellar (($\alpha_2 + \gamma$) and ($\gamma + \gamma$)) colonies. The effect of strain rate and temperature domain on hot deformability of the alloy has been analyzed through a correlation between the apparent activation energy, deformation process maps, and associated microtextural development. The relatively higher apparent activation energy ($Q = 553.8$ kJ/mol) could be correlated with the fully lamellar $\alpha_2 + \gamma$ microstructure which posses greater resistance to the mobile dislocation. The results are further corroborated by the "instability-dominated" processing maps indicating poor hot deformability of the alloy in the studied temperature–strain rate range. Detailed electron microscopy of the deformed samples indicates that poor workability exhibited as cracks that are predominantly found at the coarse γ-TiAl grains situated at the lamellar boundaries. The crack initiation and propagation mechanisms during hot compression have further been discussed with reference to concurrent dynamic recrystallization. It has been found that "wedge-type" cavitation damage is prevalent during compressive deformation in the temperature range studied here. Such cracking behavior is elucidated in light of the "Semiatin–Seetharaman criterion."

Keywords TiAl-based alloy · Hot compression · Process maps · Microstructure · EBSD · Wedge cracking

1 Introduction

The γ-TiAl-based alloys are of great interest in high-temperature applications due to their high specific strength, oxidation resistance (800–900 °C), high melting point (up to ~ 1450 °C), and good structural stability at high temperature [1, 2]. These alloys have shown potential to substitute Ni superalloy in the temperature range of 800–1000 °C depending upon microstructure evolution and alloying addition. However, one of the major obstacles which limited its applications is its poor hot workability [3, 4]. Single-phase γ-TiAl or alloys with multiple phases possess a very narrow hot working window which is often

proved to be impractical and cost-intensive for commercial exploitations [3].

In recent years, the research attention has been more shifted toward high-Nb-based γ-TiAl alloys, the so-called third-generation alloys, with Nb content in the range of 5–10 at.%. These alloys exhibit significant improvement in the strength and creep and oxidation resistance so much so that Nb has now become an essential alloying element to γ-TiAl-based multi-phase alloys. The highest amount of Nb addition reported in the literature is 10 at.% [4], which shows very high strength. The Nb addition results in further improvement in the mechanical properties by decreasing the stacking fault energy and enhancement in the oxidation resistance of the alloy at high temperature. In a recent study

[5], a poly-synthetically twinned Ti–45Al–8Nb single crystal fabricated with aligned lamellar orientation shows superior creep resistance properties, and the results open up the window for studying the material for high-temperature aerospace applications. However, the very poor hot workability remains one of the major areas of concern for the successful application of high-Nb-containing alloys. In another study, hot deformation behavior of a similar cast alloy has been characterized at various temperature and strain rates, but workability aspect of the alloy is largely ignored [6]. Hence, the reasons for poor hot workability of high-Nb-containing γ-TiAl alloys are not fully understood yet.

In this study, hot deformation behavior of a high-Nb-containing alloy (Ti–45Al–8Nb) has been explored in two phase fields (γ-TiAl + α$_2$-Ti$_3$Al) with a special emphasis to investigate the microstructural attributes to their poor workability.

2 Experimental procedure

The experimental alloy having a nominal composition of Ti–45% Al–8% Nb was produced by vacuum arc melting furnace with a non-consumable tungsten electrode in the form of pancake (dimension: ϕ100 mm diameter and 15 mm thickness). The alloy was melted to obtain pancake ingot, and the process was repeated six times by turning over the sides to ensure chemical homogeneity. The chemistry of the analyzed alloy is given in Table 1 and indicates excellent agreement with the desired nominal composition. The oxygen, nitrogen, sulfur, and hydrogen content was analyzed as 1200 ppm, 20 ppm, 170 ppm, and 28 ppm, respectively, by glow discharge optical emission spectroscopy (GD-OES).

Hot compression specimens of 12 mm length and 8 mm diameter were machined from the as-cast alloy (pancake). The opposite faces (top and bottom) of the cylindrical specimens were carefully ground to maintain parallelism and the cylindrical surface was polished to remove any surface scratches prior to testing. Hot compression tests were conducted in Gleeble 3800 at three temperatures (1273 K, 1373 K and 1473 K) and at three strain rates (0.5, 0.05, and 0.005 s^{-1}) and followed by forced air quenching. For all the test conditions, the compressive deformation was carried out up to 45% reduction in sample height. The true stress–true strain curves were calculated from the load extension data using a standard module available in the Gleeble data processing software module. The raw data were further corrected

for friction effects. From the postdeformation sample dimension, the barrelling parameters could be obtained to assess the magnitude of friction coefficient value [7]. From the estimated friction coefficients under all testing conditions, an average value of the friction coefficient was obtained. The flow curves were corrected for frictional effects by a procedure described by Evans and Scharning [8]. Gleeble-3800 simulator has a closed-loop sample current feedback-based resistive heating system, and hence, adiabatic temperature rise is minimized.

The microstructure evaluation was carried out in cast condition and after hot compression by scanning electron microscopy (SEM), X-ray diffraction analysis (XRD), electron backscatter diffraction (EBSD), and transmission electron microscope (TEM). Postdeformation microstructures of all the samples were examined at the mid-regions of longitudinal sections. The samples for metallographic analysis were prepared by standard mechanical polishing technique and Kroll's reagent (3:1 ratio of HNO3 to HF in water) was used as an etchant for the as-cast alloy. For EBSD study, the final polishing was carried out in Buehler vibratory polisher (Vibromet 2) for 12–18 h using non-crystallized colloidal silica (0.05 μm) in dilute solution. TEM samples were prepared by cutting a thin slice using a low-speed saw (Isomet, Buehler make) and then mechanically grinding up to 80 μm using fine emery paper of grit sizes from 1000 to 2500 (in P scale). Final polishing was carried out by twin-jet electropolishing (Tenupol 5, Struers make) using electrolyte of 5% H$_2$SO$_4$ and 95% methanol at 228 K.

The microstructural characterization was carried out in Zeiss EVO18 SEM at 20 kV. XRD studies were undertaken in order to identify the alloy phases present in as-cast and hot-deformed materials using a PHILIPS PW1710 automatic diffractometer. The EBSD acquisition had been done in Zeiss FEGSEM SUPRA 55 model with attached *Oxford Nordlys* EBSD detector and data analysis have been done in TSL 8.0 software. The quantification of dynamic recrystallized grain size was measured using a suitable partition function. Before applying the function, the orientation images were cleaned by using pseudo-symmetry module in TSL software to remove the pseudo twins of $60°\langle-11\,1\rangle$, $90°\langle010\rangle$, and $70°\langle1-10\rangle$ [9]. This is essential as pseudo-symmetry-related indexing problem in γ-TiAl arises due to its close tetragonal **c:a** ratio of 1.018. As a consequence, the generated Kikuchi patterns with a pseudo-cubic configuration results in indexing inaccuracies, commonly with 60° orientation solution errors about the primary prismatic axes [9]. These errors show the same misorientation as boundaries between real γ-TiAl lamellae causing additional problems revealing the true microstructure. TEM characterization was carried out using the FEI Tecnai G2 microscope operating at 200 kV.

Table 1 Chemical composition TiAl alloy in atomic percentage (wt.% in parenthesis)

| Ti	Al	Nb
46.16 (52.60)	45.65 (29.30)	8.19 (18.10)

3 Results

3.1 The as-cast microstructure

The microstructural characterization of Ti–45Al–8Nb alloy in the as-cast state is displayed in Fig. 1. The solidification of the alloy occurs via the β-phase field as predicted in the Ti–Al–Nb phase diagram [10]. At low magnification (Fig. 1a), the optical microstructure from the mid-region of the pancake shows a non-uniform distribution of the colonies with intermittent near-equiaxed γ grains. The presence of bright contrast in SEM (marked by arrowheads in Fig. 1c) is found to be "Nb-segregation" in the inter-dendritic channels. The $(α_2 + γ)$ and $(γ + γ)$ lamellar microstructure mostly observed in the band contrast image of EBSD (Fig. 1c). The microstructures examined through SEM and EBSD confirm that this alloy composition has a fully lamellar structure with a mean colony size of 530 μm. There is a large scatter in colony size ranging from 180 to 790 μm. The presence and distribution of phases are characterized through the phase map of EBSD and further confirmed by the

X-ray diffraction pattern shown in Fig. 1d. Quantitative phase analysis by EBSD phase map plot shows that the average volume fraction of γ, $α_2$, and β-phases are 95%, 4.82%, and 0.83%, respectively. Previous studies have shown that the lamellar structure consists of different type of interfaces such as $(α_2 + γ)$ or $(γ + γ)$ depending on the alloy composition [11]. The types of interfaces in the lamellar structure of each colony can be seen in the EBSD phase map (Fig. 1b, c).
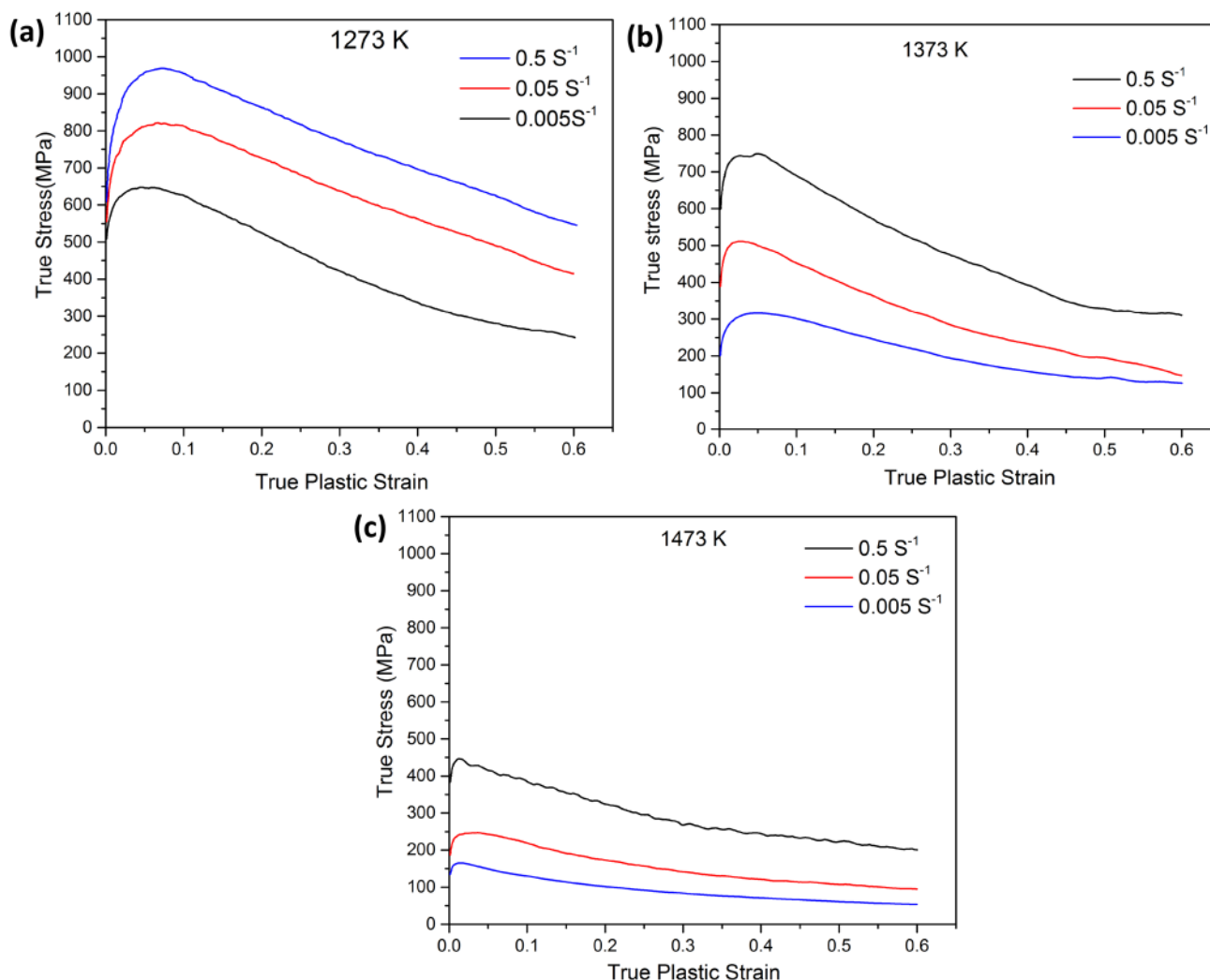
3.2 Flow behavior

The hot deformation behavior of the alloy has been studied by the hot compression tests in the temperature range of 1000–1200 °C employing a strain rate range of 0.5–0.005 s^{-1}. The flow curves obtained through hot compression tests are shown in Fig. 2. As observed in previous studies, the flow stress is found to be very sensitive to forming temperature and strain rate. With the increasing temperature and decreasing strain rate, the flow stress decreases significantly. Such flow behavior of the alloy is typical of a low-stacking-fault-energy (SFE) material [4, 12].
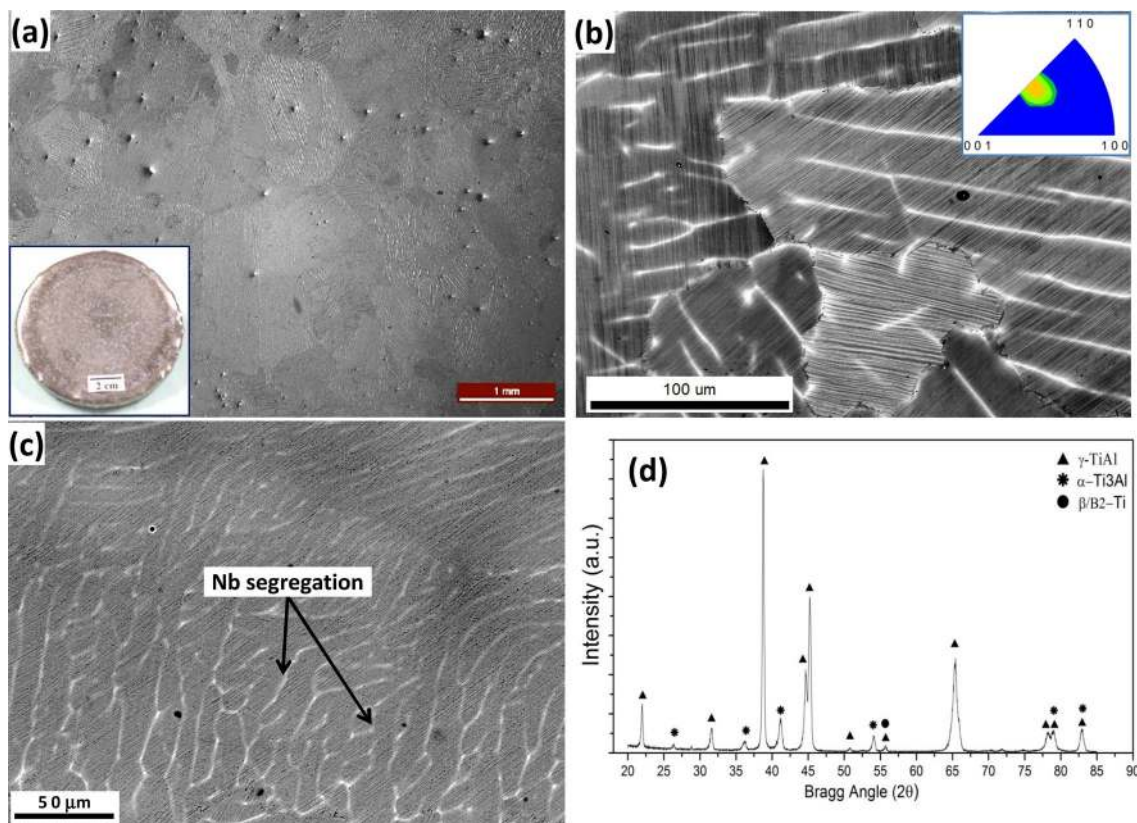
Fig. 1 **a** Optical image of the as-cast pancake showing non-uniform size distribution of colonies, **b–c** back-scattered SEM image showing microstructural features. **d** A representative XRD pattern of the as-cast alloy. **a**—inset: photograph of the pancake, **b**—inset: the inverse pole figure in Z–direction

Fig. 2 True stress–true strain curves of the experimental alloy deformed at **a** 1000 °C, **b** 1100 °C, and **c** 1200 °C as a function of strain rates

It is widely accepted that the effect of deformation temperature and strain rate on flow behavior can be expressed in terms of the Zener–Hollomon parameter (Z) [13]. A constitutive equation proposed by Sellars and McTegart [14] describes the relationship between the flow stress and the deformation parameters and is applicable to a wide range of metals and alloys including γ-TiAl alloys. It considers the flow behavior of materials during deformation as a thermally activated process and is expressed as

$$Z = \dot{\varepsilon}\exp\left(\frac{Q}{RT}\right) = A[\sinh(\alpha\sigma)]^n \quad (1)$$

where **Z** is Zener–Hollomon parameter, $\dot{\varepsilon}$ is the strain rate, σ the flow stress, Q the apparent activation energy of deformation (kJ/mol), **R** is the molar gas constant (= 8.314 J/mol K), **T** is an absolute temperature of deformation (K). **A**, **n**, and **α** are material constants. The apparent

activation energy can be calculated by partial differentiation of Eq. (1)

$$Q = R\left\{\frac{\partial\ln\dot{\varepsilon}}{\partial\ln\left[\sinh(\alpha\sigma)\right]}\right\}_T \cdot \left\{\frac{\partial\ln\left[\sinh(\alpha\sigma)\right]}{\partial(1/T)}\right\}_{\dot{\varepsilon}} \cdot \quad (2)$$

Figure 3 displays the various plots showing linear relationships between appropriate forms of peak stress, strain rate, and deformation temperatures. The apparent activation energy for hot deformation is obtained through the mean slopes of ln[sinh($\alpha\sigma$)] versus 1/T plots (Fig. 3c). Based on the analyzed data, **α** value is obtained as 0.0022 MPa^{-1}, and the average activation energy of hot deformation for Ti–45Al–8Nb alloy is estimated to be 553.8 kJ/mol. The material constants of Eq. (1) are further obtained from the logarithmic plots of Zener–Hollomon parameter (Z) versus hyperbolic sine function of
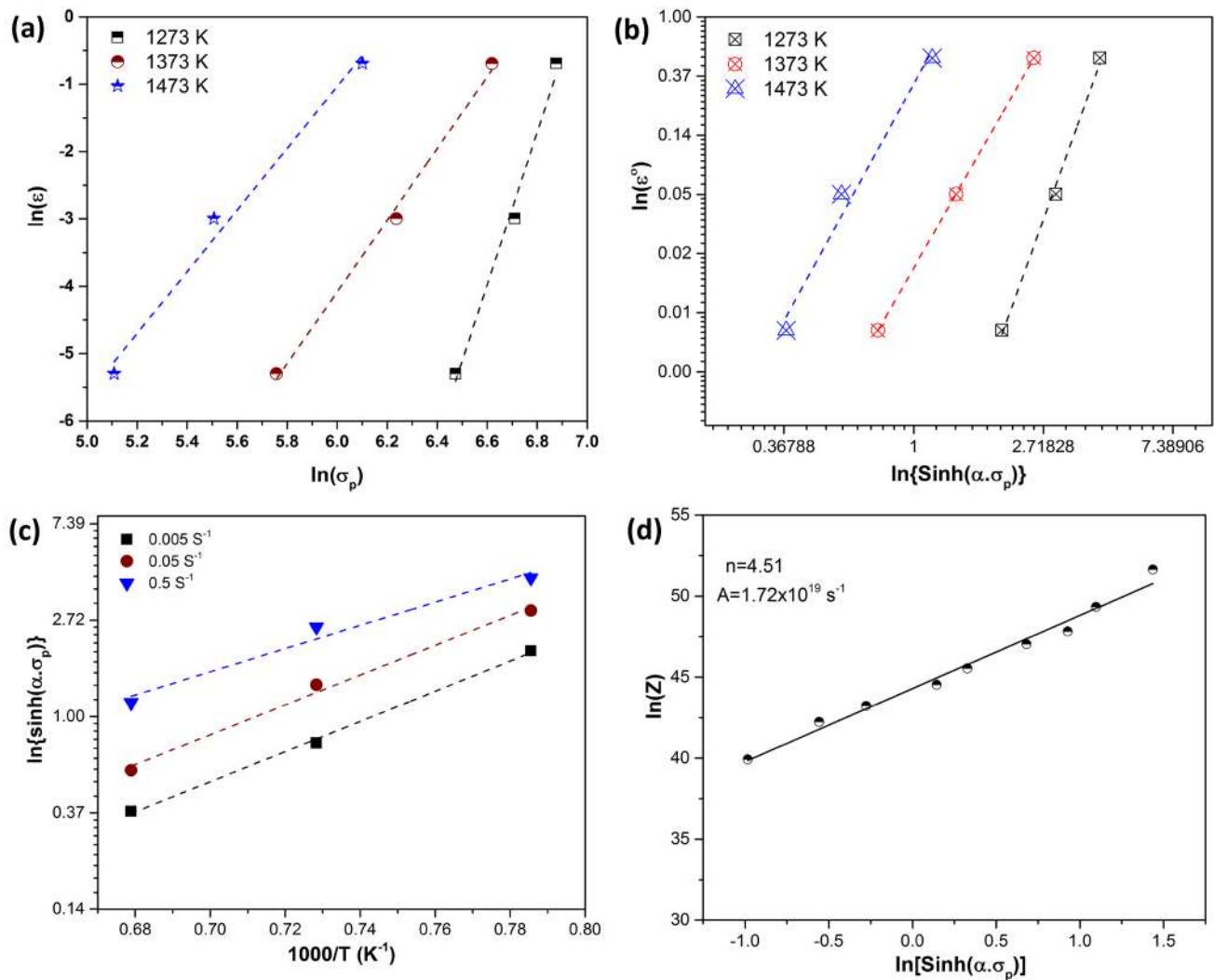
Fig. 3 Determination of constants of constitutive behavior (Eq. 1) from the linear relationships of **a** $\ln(\dot{\varepsilon})$ versus $\ln(\sigma_p)$, **b** $\ln(\dot{\varepsilon})$ versus $\ln[\sinh(\alpha \cdot \sigma_p)]$, **c** $\ln[\sinh(\alpha \cdot \sigma_p)]$ versus $1000/T$, and **d** $\ln(Z)$ versus $\ln[\sinh(\alpha \cdot \sigma_p)]$

compensated peak stress ($\alpha\sigma_p$). Figure 3d shows a linear relationship, and from linear regression, the values of **A** and **n** can be estimated as 1.72×10^{19} s^{-1} and 4.63, respectively. Therefore, the constitutive equation of hot deformation of Ti–45Al–8Nb alloy at peak stress can be expressed as

$$\dot{\varepsilon} = 1.72 \times 10^{19} \left[\sinh(0.0022.\sigma)\right]^{4.63} \exp\left(-\frac{553800}{RT}\right). \quad (3)$$

3.3 Workability of material

The visual inspection of the as-deformed samples reveals that the macroscopic deformation behavior of the alloy is highly sensitive to both strain rate and deformation temperature. For the entire range of deformation temperatures (1000–1200 °C) and strain rates (0.5–0.005 s^{-1}), the

macroscopic cracks have been observed on the bulging surface of the samples as shown in Fig. 4. It signifies the poor hot workability of the alloy at the studied temperatures and strain rate ranges. Both macroscopic surface cracks and internal cracks have been observed at high strain rate (0.5 s^{-1}) for all temperatures. The damage is particularly severe at 1000 °C and 0.5 s^{-1}, wherein surface cracks combine to propagate the entire cross section similar to the shear fracture. On the other hand, at slow strain rates and higher temperatures (1100–1200 °C), cracks are found mostly on the outer bulge surface and no cracks are noticed in the cross-sectional microstructure of the postdeformed samples.

In order to analyze the hot deformability in quantitative sense of the present alloy during hot deformation, the experimental flow stress data have been analyzed using the dynamic material model (DMM) technique
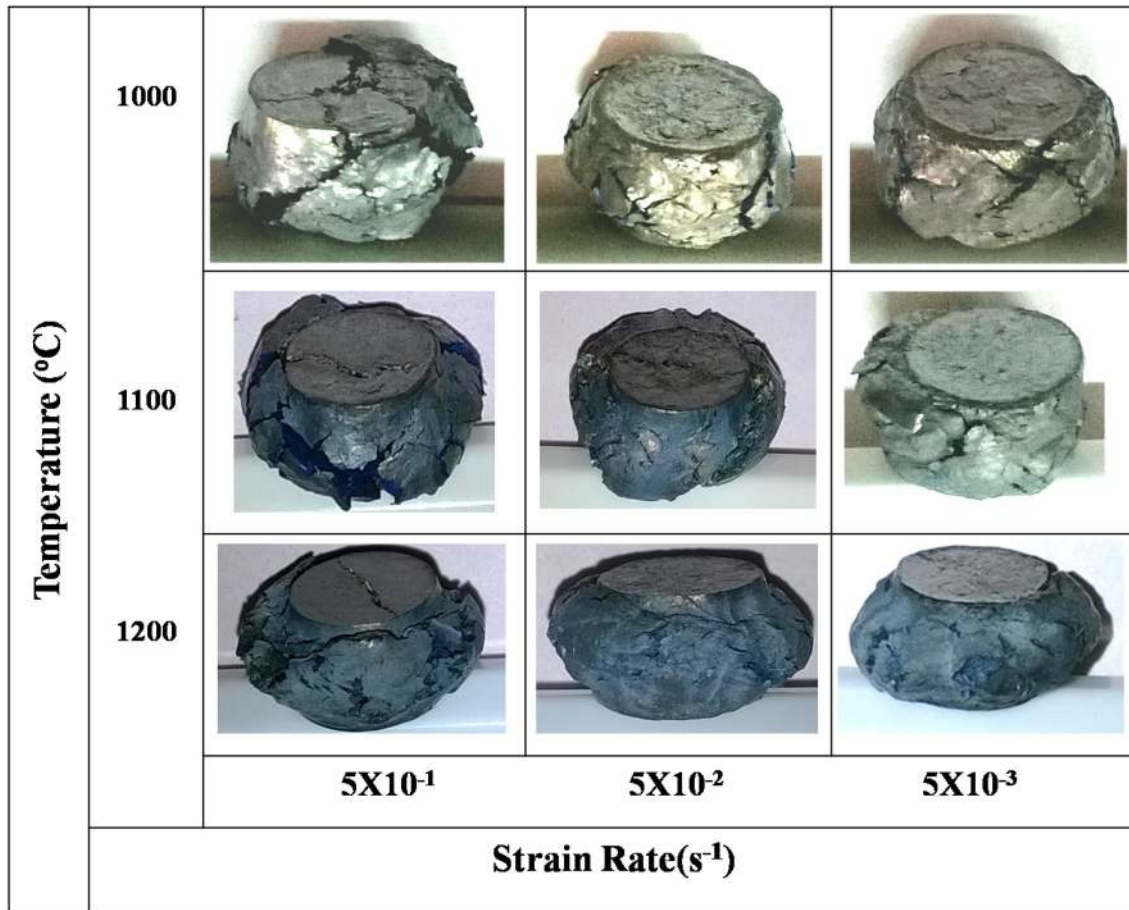
Fig. 4 Macroscopic view of compression tested sample as functions of temperature and strain rate

pioneered by Prasad et al. [15]. In the DMM model, the microstructural changes during hot deformation have been considered to find out the safe limit for processing domains of metals and alloys [15, 16].

The power dissipation efficiency maps obtained for the Ti–45Al–8Nb alloy over the experimentally employed temperature and strain rate are shown in Fig. 5. The efficiency maps are constructed at true strains of 0.2, 0.4, and 0.5. The black contours in the maps denote the efficiency lines, which are directly related to the evolution of microstructure, whereas the red lines show the instability region, which shows negative value at the temperature range of 1000–1200 °C in the low strain rate. It is also seen that at the highest strain rate (0.5 s^{-1}) instability dominates for the entire temperature range, which is confirmed by the poor workability of the material (Fig. 4). It has been observed that at logarithmic stain rate value at -2.5 to -3.5 and deformation temperature between 1150 and 1200 °C, the efficiency value is near to 50–55 in all three maps, which is presumed to have good workability. However, both the macroscopic and

microscopic examination of as-deformed specimens shows the presence of deformation induced defects.

3.4 Microstructure after deformation

Figure 6 summarizes the postdeformation microstructural developments in the samples deformed in the temperature range of 1000–1200 °C and strain rate of 0.5–0.005 s^{-1}. It is clear that deformation temperature and strain rate have a profound effect on the development of microstructures. Following hot compressive deformation, the lamellar initial microstructure undergoes three major changes depending on the strain rate and temperature which includes: (1) changes in phase fraction, (2) formation of equiaxed dynamically recrystallized grains, and (3) bending (kinking) of lamellar colonies and evolution of shear bands. The dynamic recrystallization has been found to occur by heterogeneous nucleation as most of these DRX grains are observed at prior colony boundaries and within the colony at lath boundaries. The variations in DRX fraction and grain growth of both α_2, and γ phases in the
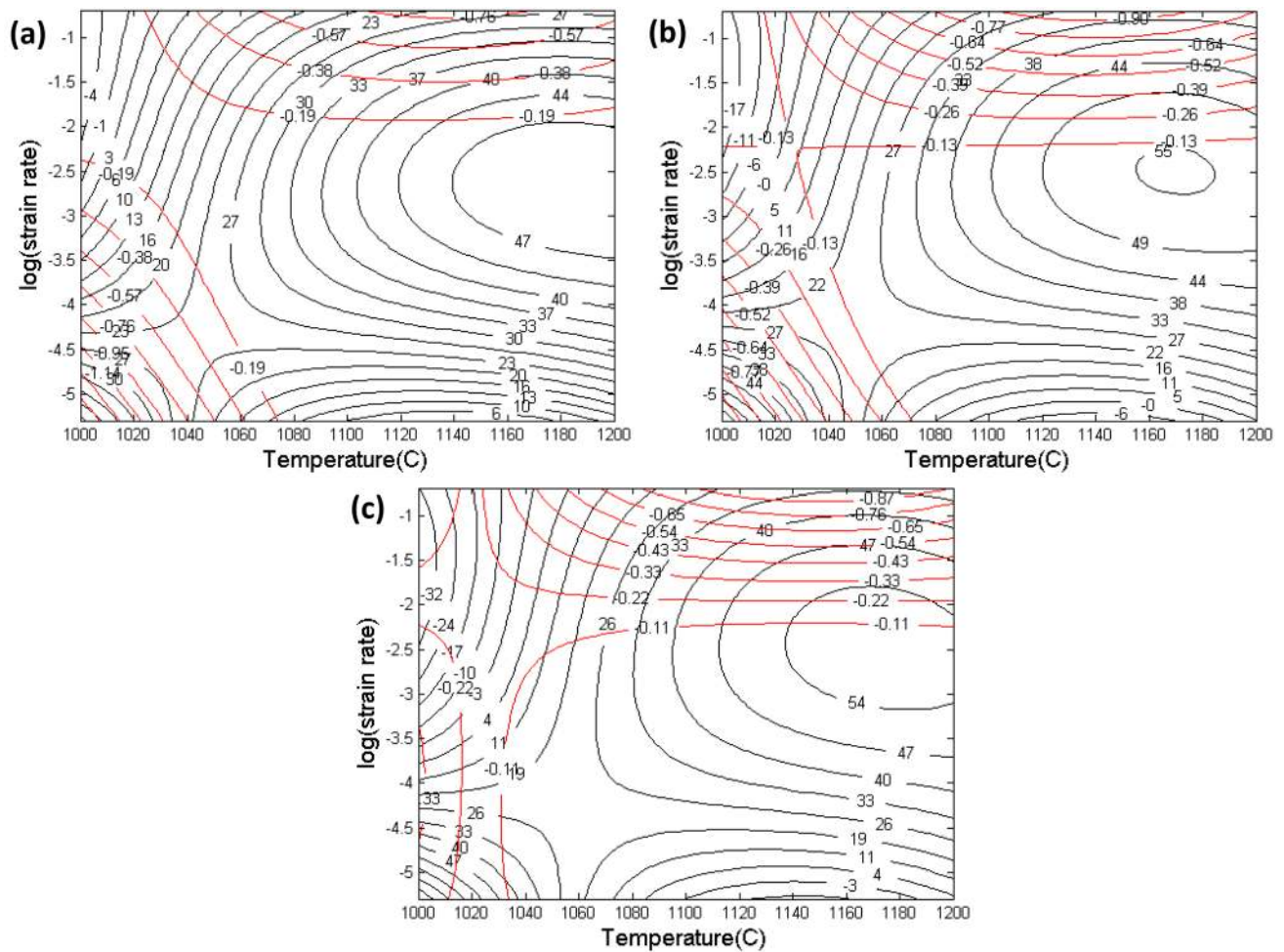
Fig. 5 Power dissipation efficiency map superimposed with instability as a function of temperature and strain rates at a true strain of **a** 0.2, **b** 0.4 and **c** 0.5

alloy are strongly affected by strain rate and temperature. In addition, detailed microstructural characterization using EBSD also reveals the presence of defects in the postdeformed samples. Characterization of defects is displayed in Fig. 7 as a function of deformation parameters. It could be readily noticed that inter-lamellar cracks are predominant for deformations at high strain rates (0.5, 0.05 s^{-1}) irrespective of temperature and even at the slowest strain rate (0.005 s^{-1}) with a lower temperature of deformation (1000 °C) as shown in Fig. 7a–c. However, deformation at the highest temperature and lowest strain rate (1200 °C, 0.005 s^{-1}) favors a typical "wedge"-type cracking at intra-lamellar locations (Fig. 7d).

3.4.1 EBSD characterization

The DRX microstructure evolution as a function of temperature and strain rate is shown through EBSD in band contrast maps (Fig. 8). It is evident that DRX fraction increases

with increasing temperature and decreasing strain rate. It is also accompanied by changes in the phase fraction of γ-TiAl and α_2-Ti$_3$Al significantly as shown in phase maps (Fig. 8, insets). For deformation at 1200 °C (above the eutectoid temperature), the α_2-Ti3Al phase fraction (color-coded as blue regions) increases sharply with a concomitant decrease in γ-TiAl phase (color-coded as red regions). It is clear that very few sub-microscopic size DRX grains have formed at prior lamellar colony boundaries at high strain rate (0.5 s^{-1}) and lower deformation temperatures (1000, 1200 °C) as shown in Fig. 8a, c. On the other hand, well-developed DRX grains with increase in grain size are formed at a low strain rate of 0.005 s^{-1} at 1000 °C and 1200 °C temperature (Fig. 8b, d). However, for all the deformation conditions, remnant colonies of lamellar structure could be noticed in the microstructure (Figs. 6, 8). A careful examination of the microstructures indicates that the remnant colonies are having lamellar orientations between 45° and 90° to the compression axis. It has been found that the
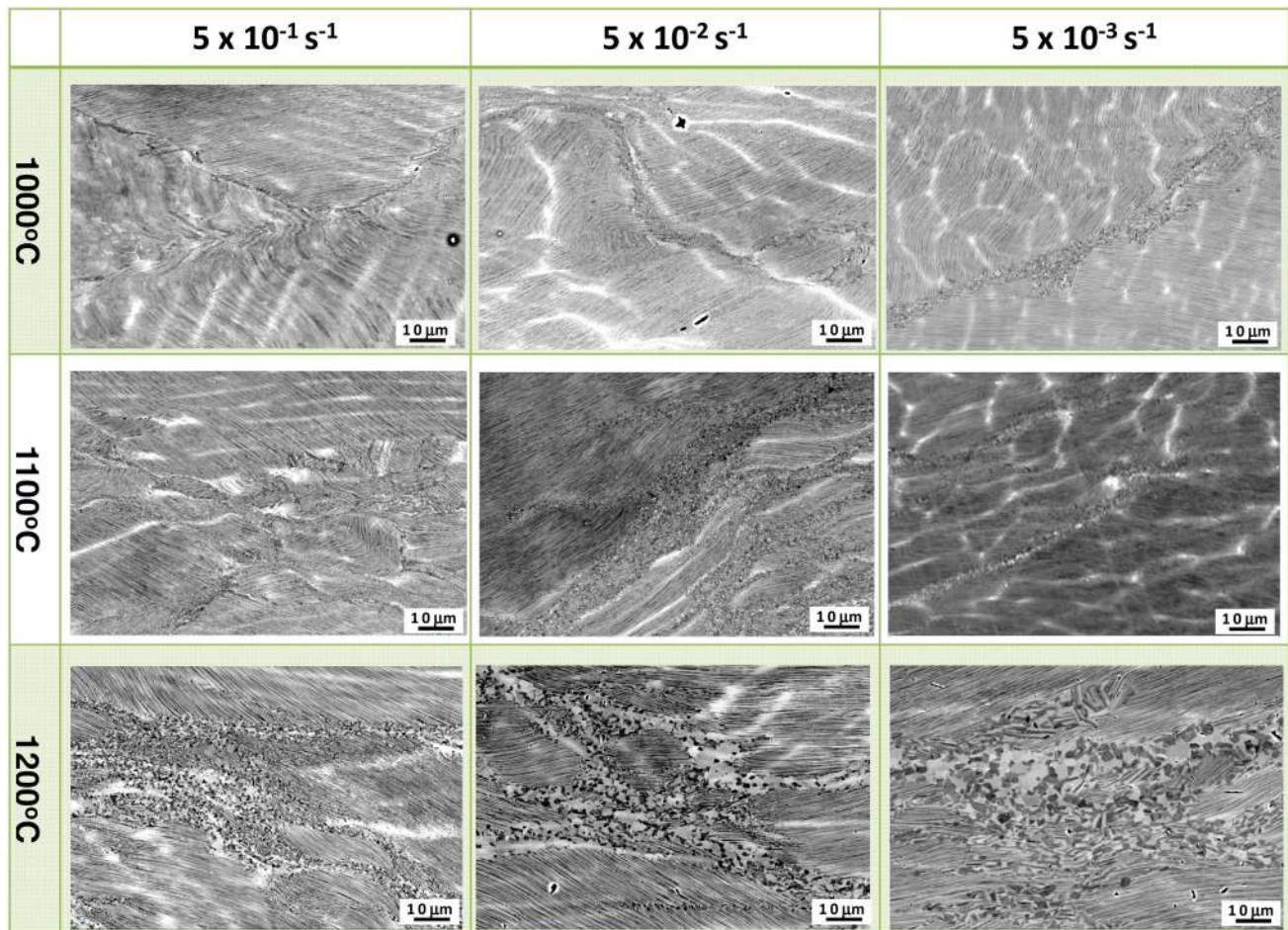
Fig. 6 A matrix of post-deformation microstructures imaged in BSE mode as a function of deformation temperature and strain rates

lamellae which are oriented more than 45° to the compression axis are less prone to dynamic recrystallization due to lack of cross-twining and the rotation modes. On the other hand, colonies with the lamellar orientation of 0° to the compression axis are the most favorable for dynamic recrystallization as intensive cross-twining and activation of rotation modes during initial loading promote the DRX and/or spheroidization. Similar results have also been observed during hot deformation of Ti–48Al–2Cr alloy by Salishchev et al. [17].

4 Discussion

4.1 High-temperature deformation behavior

It is evident from the results presented in the previous section that the hot deformation behavior of high-Nb-containing γ-TiAl alloy is characterized by large activation energy, and thus, the flow stress is strongly affected by the temperature and strain rate. The measured value

of apparent activation energy ($Q = 553.8$ kJ/mol) for the present alloy is considerably higher than the activation energy of Ti–Al inter-diffusion (298 kJ/mol), Ti self-diffusion (260 kJ/mol), and Al self-diffusion (360 kJ/mol) in single-phase γ-TiAl alloys [18, 19]. The result implies that diffusion-assisted deformation processes are impeded in such alloys. The higher value of apparent activation energy could, therefore, be associated with solid solution hardening due to higher Nb content and the presence of secondary phases ($α_2$). However, considering the dislocation dynamics of these multi-phase materials with lamellar microstructure, it has been widely observed [4] that lamellar $α_2 + γ$ microstructure posses greater resistance to the mobile dislocation since $α_2/γ$ interface acting as a strong barrier (Fig. 9a). Hence, the lamellar $α_2 + γ$ microstructure is more likely to contribute to the high activation energy to hot deformation of the present alloy. It is well corroborated with the similar values reported in the literature for Ti–45Al–5Nb–0.2B–0.2C, Ti–45Al–8Nb-0.2C, and Ti–45Al–10Nb alloys having initial near-lamellar microstructure [4].
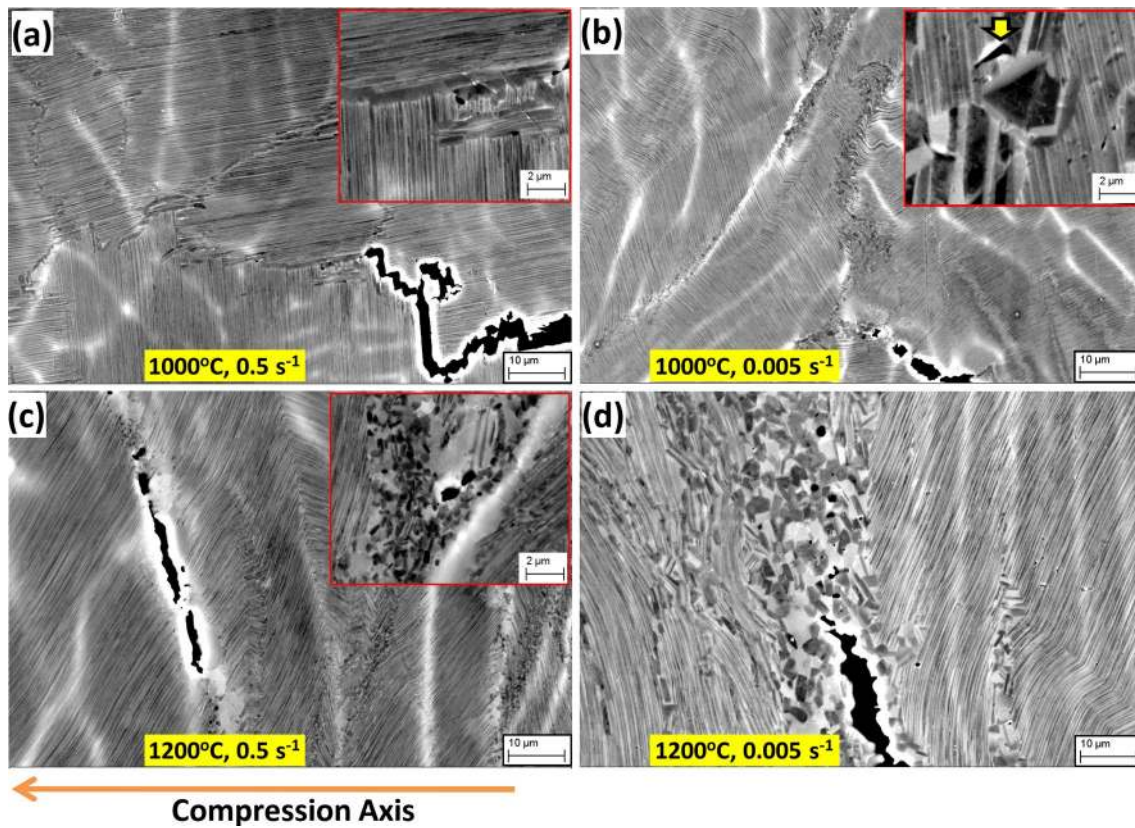
Fig. 7 BSE images of sample deformed to a true strain of 0.6 under the deformation conditions of **a** 1000 °C, 0.5 s^{-1}, **b** 1000 °C, 0.005 s^{-1}, **c** 1200 °C, 0.5 s^{-1}, and **d** 1200 °C, 0.005 s^{-1} showing the effect of microstructural development on the cracking tendencies. Inset: high-magnification BSE images showing origins of cracking. For all the images, the compression axes are horizontal

The apparent difficulty in hot deformability of the alloy is further reflected in the processing maps as shown in Fig. 5 at different levels of plastic strains. The processing maps constituted with superposition of power dissipation and instability maps evoke different domains of deformability corresponding to dominant micromechanism of deformation. It is generally believed that good hot workability and stable flow of a material are typically associated with dynamic softening mechanisms such as recovery and recrystallization corresponding to the power dissipation efficiency values of 30–40% [20]. It is to be noted that the domains of high power dissipation efficiency (~ 1170–1180 °C, 0.08–0.05 s^{-1}) as shown in processing maps are close to the instability zones and, thus, do not correspond to "safe" hot processing zone as verified by hot compression test results. It indicates that the higher values of power dissipation could not be attributed to dynamic recovery and/or recrystallization processes; rather, it may be associated with the formation of cracks during deformation since sample cracking utilizes a considerable amount of energy in creating new crack surfaces [20]. The postdeformation microstructural evolution in the instability-dominated zones suggests the non-uniform deformation with severe kinking and bending of lamellar colonies (Fig. 6). The very fine-grained recrystallized layer developed near colony boundaries (for temperature ~ 1200 °C) is believed to be initiated at later stages of deformation indicating lack of dynamic softening mechanism at the initial stages of deformation. It is consistent with the fact that recovery process is highly hindered in the high-Nb-containing fully lamellar γ-TiAl alloys due to their significantly low stacking fault energy and the presence of impenetrable α$_2$/γ interfaces [4].

4.2 Effect of initial microstructure and texture

Apart from the strong covalent-type directional bonding of γ-TiAl-based intermetallics, one of the crucial factors controlling the "technological plasticity" of cast alloys is microstructure together with chemical homogeneity and solidification texture [21]. For good hot workability of γ-TiAl-based alloys, a cast ingot with refined grain structure, good chemical inhomogeneity, and the absence of sharp solidification texture is found to be beneficial [4, 22]. For cast TiAl-based alloys, these favorable microstructural features are generally achieved through the so-called
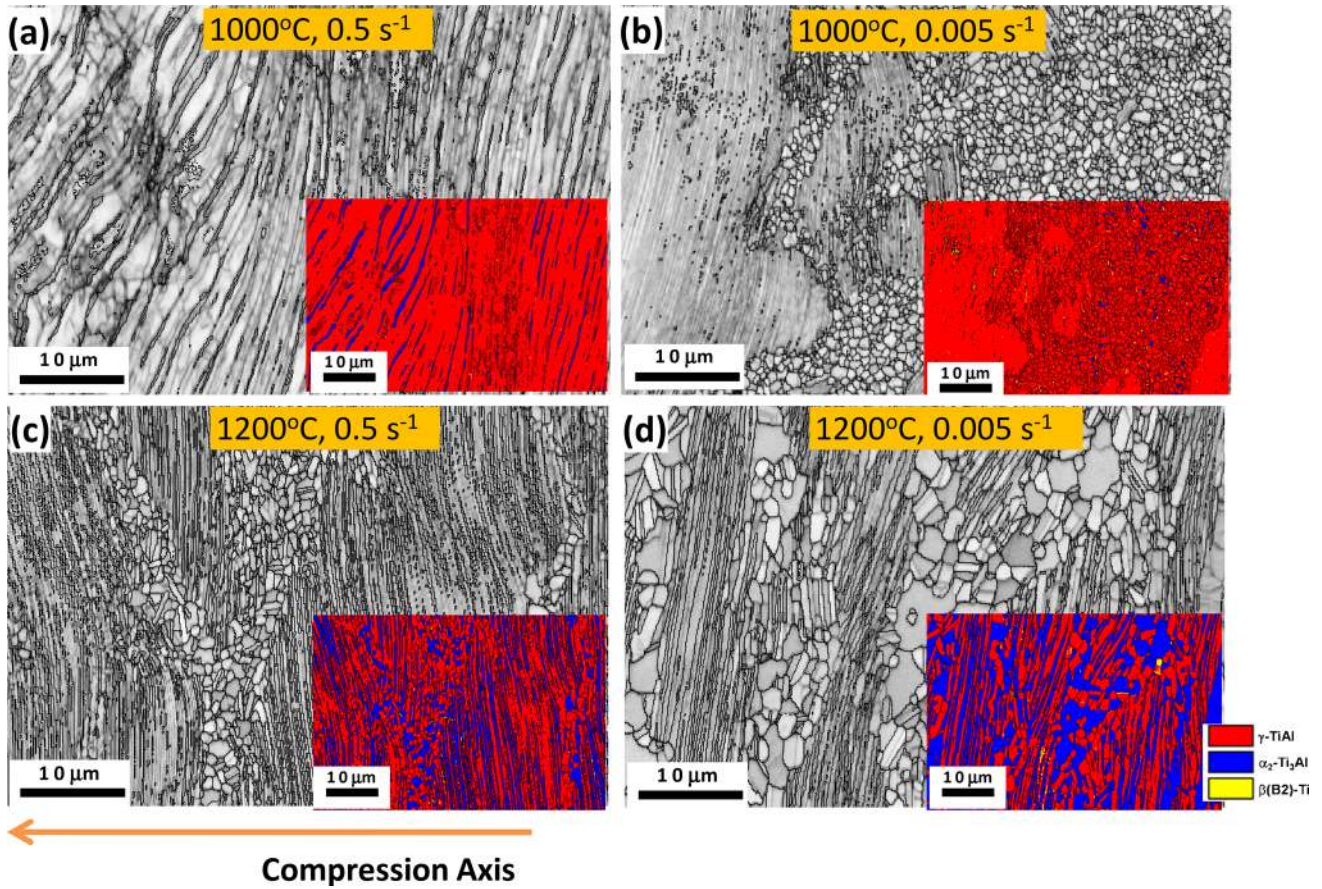
Fig. 8 High-magnification EBSD band contrast images showing microstructural development in samples deformed at **a** 1000 °C, 0.5 s^{-1}, **b** 1000 °C, 0.005 s^{-1}, **c** 1200 °C, 0.5 s^{-1}, and **a** 1200 °C, 0.005 s^{-1}. Insets: corresponding phase maps. For all the images, the compression axes are horizontal
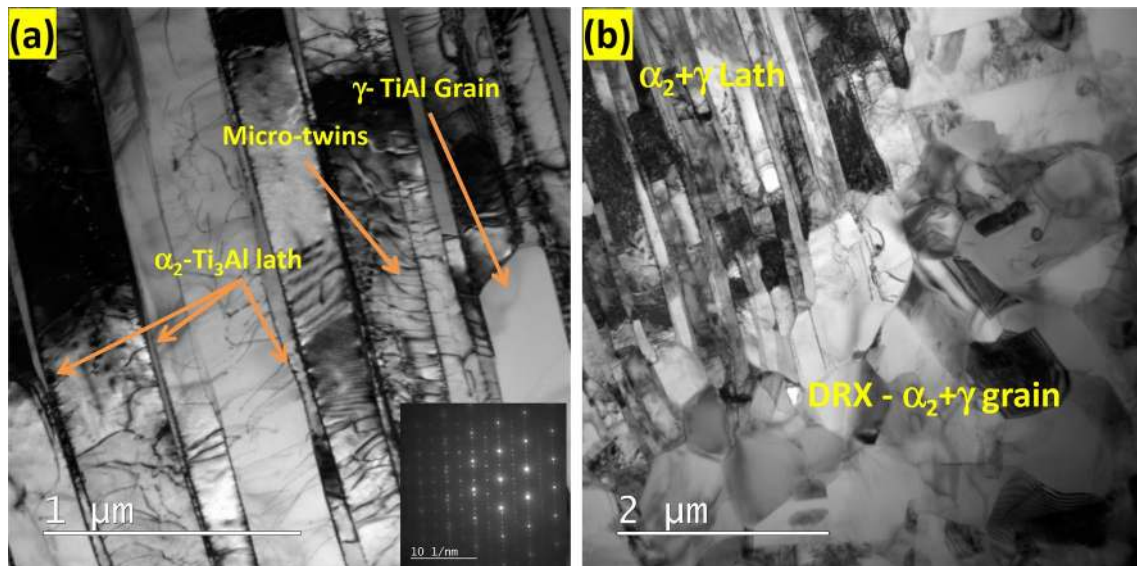
Fig. 9 Bright-field TEM images of samples deformed at 1000 °C, 0.005 s^{-1}: **a** deformation mechanism and **b** prevailing DRX mechanism

β-solidifying alloys [23]. Although the phase diagram [8, 24] of the present alloy system (Ti–45Al–8Nb) suggests it to be a β-solidifying alloy, the beneficial microstructural features could not be obtained in the pancake used in the present study. The as-cast microstructure of the present alloy consists of fully lamellar $\alpha_2 + \gamma$ colonies with a very large average colony size, but relatively finer lamellar spacing. It could probably be associated with absence of boron as grain refiner as the colony size tends to be coarse in B-free alloys [4]. It is generally observed that with the increase in α_2 volume fraction induced by lower Al concentration of the alloy the lamellar spacing tends to be finer [4]. The adverse effect of very coarse colony size is further accentuated by the presence of strong solidification texture (Fig. 1). As mentioned previously, a strong $\langle 111 \rangle_\gamma$ texture parallel to the radial direction of the pancake is formed due to pronounced dendritic solidification along the direction of heat flow [25]. Such strong texture development is particularly detrimental to hot workability of the TiAl alloys due to the asymmetry of the four ordinary slip systems that are relatively easy to activate in two-phase TiAl alloys compared to the eight $\langle 101 \rangle$ super-dislocation systems [25]. The interpretations corroborate well with the poor hot workability of the present alloy, especially at lower temperatures (1000–1100 °C). At higher temperatures (1200 °C), the workability is marginally improved, particularly at lower strain rate, due to increased propensity of twinning (Fig. 8b) and reduced plastic anisotropy of γ-TiAl phase with active contributions of $\langle 010]$ dislocations [26].

In addition, the as-cast microstructure shows significant microsegregation of Nb. Although segregation of Nb does not seem to directly affect the hot workability of the alloy, its indirect contributions should be noted. It is possible that chemical inhomogeneity of Nb through strong dendritic segregation hinders the grain refinement as effected by $\beta \rightarrow \alpha$ transformation and high Nb addition [27].

4.3 Effect of inhomogeneous DRX

It has been found that the initial lamellar microstructures do not break down completely by thermomechanical processing at high temperatures [28]. The postdeformation microstructures consist of remnant lamellar colonies (($\alpha_2 + \gamma$) or ($\gamma + \gamma$)) interspersed with DRX grains (Figs. 6, 8). Most of these grains are in colony boundaries and lath boundary shown in TEM micrographs Fig. 9a, b. It is further noted that dislocation can be easily moved from one γ-TiAl lath to another, whereas the same is restricted in case of TiAl to Ti_3Al phase (Fig. 9a). In addition, the presence of microtwins is observed in the γ-TiAl laths, which indicates the possible contribution of twining as a mode of deformation at high temperature. These microtwins

further initiate DRX grains due to their favorable energy considerations [4].

Furthermore, the overall dynamic recrystallization is observed to be inhomogeneous and is believed to be associated with the orientation of lamellar colonies [28]. Such orientation-dependent deformation behavior of lamellar colonies plays a critical role in determining the dynamic softening in conjunction to the temperature of deformation. At lower temperature of deformation (1000 °C), extensive bending and kinking of ($\alpha_2 + \gamma$) or ($\gamma + \gamma$) lamellar colonies have been observed. Furthermore, addition of Nb significantly reduces the SFE of γ-TiAl [4] and consequently suppresses the dynamic recovery (DRV). In the absence of DRV in the high-Nb-containing alloys at lower temperatures, a state of significantly high stress concentration across the colony boundaries develops leading to wedge-type cracking at the colony boundaries. At higher temperatures (1200 °C) and slower strain rates, the stress concentration is partially accommodated by multiple twinning (and occasionally cross-twinning) and enhanced DRV as well as DRX. Such interpretations corroborate well with the experimental results that at lower temperatures the cracks mostly found to initiate and propagate along the colony boundaries (Fig. 8a, b), whereas with increasing temperatures, particularly at the lowest strain rate, intralamellar wedge cracking could be noticed with substantial reduction in cracking tendencies along the colony boundaries (Fig. 8d).

4.4 Wedge and cavitation damage

The hot workability of γ-TiAl-based intermetallic alloys is generally observed to be limited by the generation and propagation of various internal defects such as wedge cracking/cavitation and shear bands to produce macroscopic failure. High-Nb-containing TiAl alloys possess even greater challenges during thermomechanical processing.

Characterization of defects generated during hot deformation of the present alloy suggests that "wedge"-type inter-lamellar cracks are predominant in the entire deformation range (Fig. 7). Only at the highest temperature and slowest strain rate condition (i.e., 1200 °C, 0.005 s^{-1}), some globular voids/cavitation types of defects are noticed at the dynamically recrystallized area in addition to the wedge-type inter-lamellar cracks (Fig. 7d). However, a careful examination of the origin of the defects at higher magnification reveals that nuclei of both types of cracks are present under all deformation conditions (Fig. 7-insets). The cavitation types of voids are found to grow only at high temperature–slow strain rate conditions, whereas wedge-type cracks readily propagate under all deformation conditions, especially at higher strain rates. It is also noteworthy that cracks are nucleated

either at the interface between lamellar colony-γ-grains (Fig. 7a, b-insets) or at the course recrystallized γ-grains (Fig. 7c-inset). It has been proposed that grain boundary sliding plays a major role in the nucleation of both wedge cracks and cavities [29–31]. Due to the lack of adequate matrix slip and grain boundary diffusion in γ-TiAl alloys, especially at low temperature and high strain rates, grain boundary sliding leads to stress concentration at the colony boundaries and triple junctions. Wedge cracks can initiate when such stress concentrations are not effectively relieved [31].

A microtextural assessment of the cracking behavior is found to corroborate the proposed mechanism described above. Figure 10 displays the microtextural features associated with a typical cracking behavior at the low temperature 1000 °C and low strain rate 0.005 s^{-1} near the crack region. The deformation temperature (1000 °C) is well below the eutectoid point, the slip behavior of lamellar γ-TiAl is highly constrained, and the same is reflected through the band contrast image (Fig. 10b) and the associated KAM map and GOS spread of γ-phase (Fig. 10c, d). The development of stress concentration is evident near

the lath bending and kink region formed within the shear bands developed across the colonies. Figure 10c, e, f further shows the crack arrest and deflection as a result of DRX. The development of DRX (fine grains developed near the right side of the crack tip, Fig. 10f) results in minimization of misorientation (indicated by blue color code), and hence, the crack appears to be arrested and deflected to left side following a high stress concentration path.

Deformation behavior above the eutectoid temperature at 1200 °C is substantially modified with increasing cavitation type of damages and diminishing wedge-type cracking. A typical example is shown in Fig. 11. Above the eutectoid temperature, the deformation is accompanied by an increase in the volume fraction of disordered α-phase (Fig. 11a, b-insets). The development of misorientations is observed to be restricted to the lamellar boundaries within the individual colonies (Fig. 11c, d). However, the presence of relatively more deformable α-phase and occurrence of the significant amount of DRX at the colony boundaries substantially increases the deformability of the alloy. This is well corroborated with the reduction in stress concentration along the boundaries (Fig. 11c, d) and concomitant
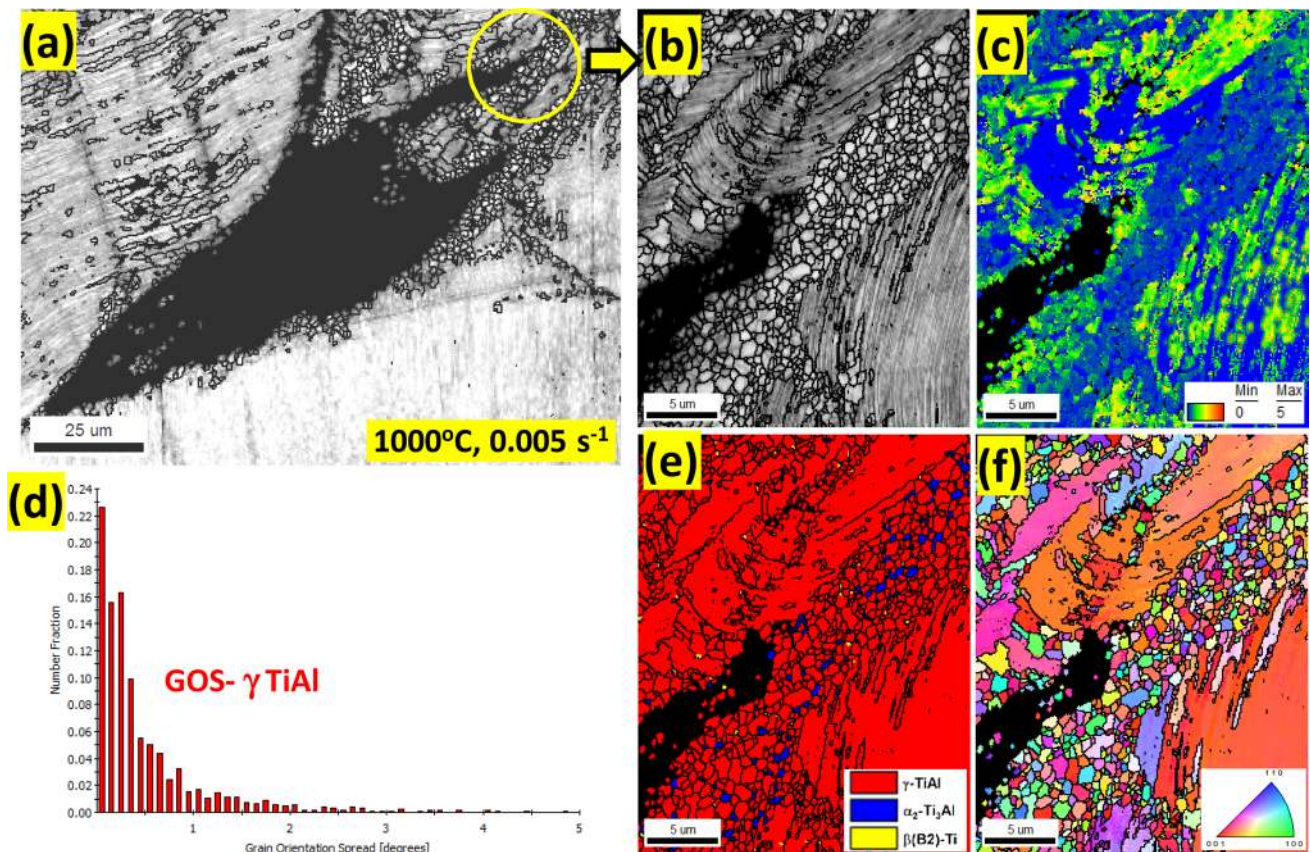
Fig. 10 EBSD characterization: **a** band contrast image at 1000 °C, 0.005 s^{-1}, **b**, **c**, **e**, **f** magnified views of area marked in **a** represented as band contrast image, KAM map, phase map, orientation image of all phases, respectively. **d** GOS chart of γ-TiAl phase of corresponding image (**a**)
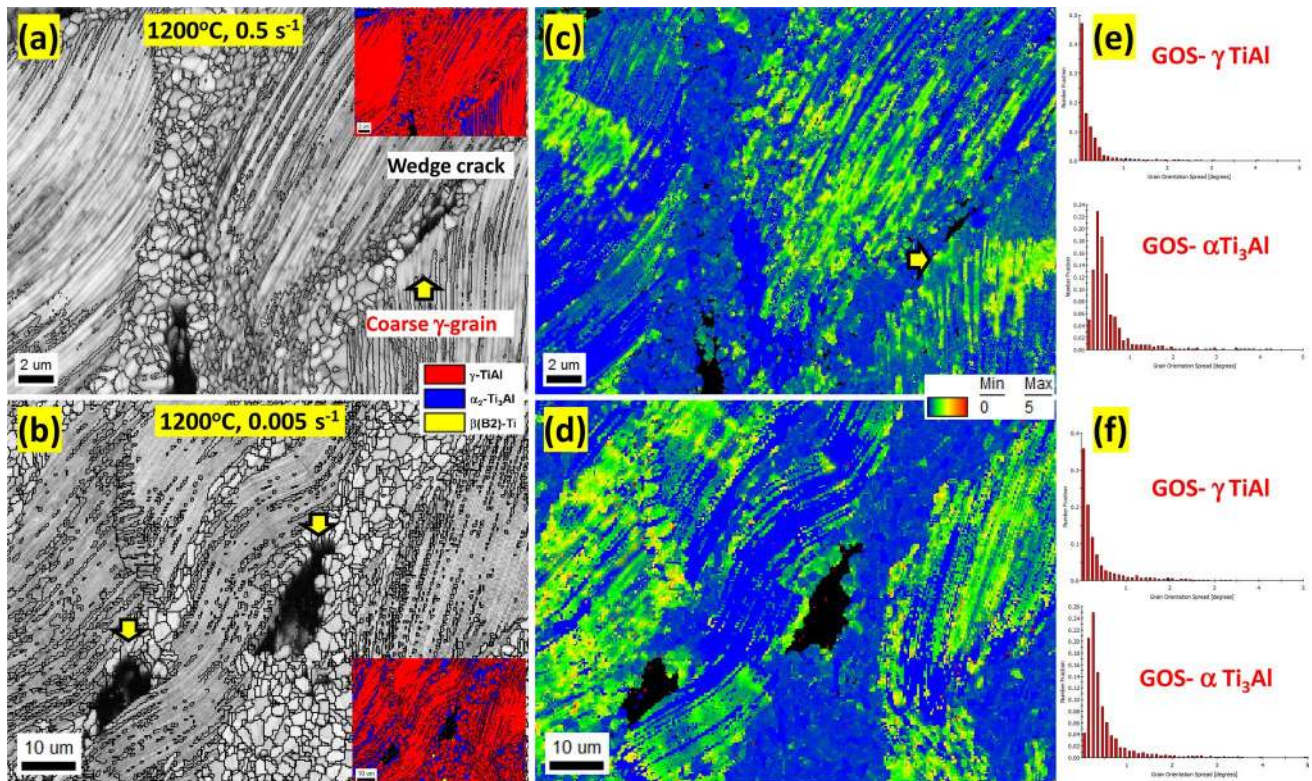
Fig. 11 EBSD band contrast images and corresponding KAM images with GOS chart of individual phases at crack region for the samples deformed at **a**, **c**, **e** 1200 °C, 0.5 s^{-1} and **b**, **d**, **f** 1200 °C, 0.005 s^{-1}. Insets: corresponding phase maps in band contrast images

reduction in wedge cracking. The relative deformability of α-phase is established through comparison of the relative GOS spreads of the γ- and α-phases, which indicate that α-phase undergoes more deformation resulting in higher misorientation spread (Fig. 11c–f). However, a few wedge cracks could still be noticed at higher strain rates (Fig. 11a). It is observed that such cracks are found to be associated with coarse γ-grain present at the colony boundaries in accordance with reported studies [31]. It is interesting to note the high strain gradient associated with such coarse γ-grain (Fig. 11c) compared to the behavior of bulk γ-phase. It is, therefore, evident that coarse γ-grains present at lamellar colony boundaries hinder the colony boundary migration and facilitate the development of stress concentration build up leading to crack nucleation.

4.4.1 Semiatin–Seetharaman criterion

The discussion on the hot workability (through process maps) of difficult to deform materials such as γ-TiAl intermetallics is often complemented with the phenomenon of initiation of fracture processes. A "critical fracture-stress"-based concept forwarded by Nobuki et al. [32] offers limited success in binary Ti–Al-based alloys. However, the concept of critical stress fails to converge to a

technologically viable concept as the wide range of the amount of deformations used in the literature creates significant scatter, especially for complex multi-component microstructures. The vast body of literature suggests that the critical fracture stress of multi-component γ-TiAl-based alloys during hot deformation is apparently controlled by the microstructural modifications effected through variations in alloying additions such as aluminum (determining α$_2$-γ two-phase structure) and β-stabilizing elements [23, 27]. In order to overcome such limitations, Semiatin and Seetharaman [31, 33] have developed a "microstructure-informed criterion" for the initiation of wedge cracking for brittle failure during hot deformation of γ-TiAl incorporating both peak flow stress (σ_p) and grain size (d). The approach relies on the critical value of the parameter "$\sigma_p\sqrt{d}$" as the criterion for wedge cracking. It is of interest to compare the present results with that of the values associated with low-to-high-Nb-containing TiAl alloys reported in the literature. The comparisons are furnished in Table 2. The calculated values of the Semiatin–Seetharaman parameter for various TiAl-based alloys imply that the transition from sound deformation to wedge/surface crack initiation occurs beyond the critical value of ~ 2.5. It is evident that the predictive capability of the said parameter is valid for the present alloy as the poor workability is well

Table 2 Semiatin–Seetharaman parameters for various γ-TiAl-based alloys

Alloy composition	Processing condition		$\sigma_p\sqrt{d}$	Remarks
	Temperature (°C)	Strain rate (s^{-1})		
Ti–45Al–8Nb [present study]	1200	0.005	3.80	Bulge cracks, no internal cracks
	1200	0.05	5.67	Bulge cracks, no internal cracks
	1100	0.005	7.28	Internal cracks
Ti–45Al–8Nb–2Cr–0.2B [34]	1200	0.005	0.60	Sound deformation
	1200	0.05	1.15	Sound deformation
	1100	0.05	1.37	Sound deformation
	1100	0.5	3.62	Surface cracks
Ti–45Al–2Nb–1.5V–1Mo–Y [35]	1200	0.01	1.49	Sound deformation
	1150	0.001	1.36	Sound deformation
	1100	0.01	2.38	Internal cracks
Ti–43.9Al–4.3Nb–0.9Mo–0.1B–0.4Si [36]	1200	0.01	0.53	Sound deformation
	1200	0.05	0.72	Sound deformation
	1100	0.5	3.83	Crack
Ti–46Al–2Cr–4Nb–0.2Y [20]	1250	0.01	1.59	Sound deformation
	1250	0.05	1.77	Sound deformation
	1175	0.01	2.55	Crack

corroborated by the significantly higher values of Semiatin–Seetharaman parameter.

4.5 Role of high-Nb alloying

The Nb addition to Ti-rich γ-TiAl alloys imparts excellent oxidation resistance and enhances the high-temperature capability of retaining high strength at higher temperatures. It significantly reduces the diffusivity of γ-TiAl alloys and increases the phase stability of both α_2 and γ-phases. It has also been reported that higher Nb addition significantly reduces the stacking fault energy (SFE) of γ-TiAl alloys [4]. This effect together with the very sluggish diffusion causes lower efficiency in hot deformation as reflected in processing maps, particularly at Nb additions > 8 at.%. It has been reported that the peak efficiency is reduced from 50–60% to 30–40% by lowering the SFE due to higher Nb addition [12]. The experimental findings on 2, 5, 8 at.% Nb-containing γ-TiAl alloys suggest that the processing window becomes progressively narrower and shifts toward higher temperatures and lower strain rates [20, 35, 37]. From the foregoing discussion, the role of high-Nb alloying toward poor hot workability of the present alloy can be illustrated through its association with (1) microsegregation, (2) insufficient DRX at the initial stages of deformation and lack of DRV at lower temperatures, and (3) higher activation energy barrier.

One of the most effective ways of improving the hot workability of the high-Nb-containing γ-TiAl alloys is to refine the cast grain/colony size and incorporate a softer β-phase by suitable alloying. It has been found that a judicial addition of Cr + B to the Ti–45Al–8Nb alloy can substantially improve the hot workability by reducing wedge-cracking tendencies [34].

5 Conclusions

The hot workability of Ti–45Al–8Nb (at.%) alloy has been studied by uniaxial compression tests in the temperature range of 1000–1200 °C and strain rate range of 0.5–0.005 s^{-1}. The following conclusion can be drawn.

1. The hot compression of the Ti–45Al–8Nb (at.%) alloy exhibit typical flow softening features sensitive to temperature and strain rate. The relatively poor hot deformability has been rationalized through of the high apparent activation energy of hot deformation ($Q = 553.8$ kJ/mol) and the stress exponent ($n = 4.63$) determined by constitutive modeling of the flow curves. It is suggested that the measured activation energy could be correlated with the solid solution hardening by Nb and the presence of lamellar ($\alpha_2 + \gamma$) microstructure.
2. The power dissipation efficiency map as a function of temperature and strain rates in conjunction with macro- and microstructural considerations indicates that the Ti–45Al–8Nb alloy has instability-dominated poor workability in the temperature range of 1100–1200 °C and strain rate range of 0.05–0.005 °C.
3. The poor hot deformability of high-Nb-containing γ-TiAl-based alloy could be attributed to combination of the factors such as (1) very coarse cast colony size with strong $\langle 111 \rangle_\gamma$ texture, (2) retarded recovery

and recrystallization aided by low diffusivity and grain boundary mobility due to high-Nb alloying, and (3) the absence of stress accommodating phase at colony boundaries.

4. Cracks developed during hot deformation are predominantly of wedge-type found at the coarse γ-TiAl grains situated at the lamellar boundaries. The initiation and propagation of cracks/cavitations are closely related to the deformation behavior of lamellar structure and concurrent dynamic recrystallization. Such cracking behavior has been found to follow "Semiatin–Seetharaman criterion" for the present alloy.

Compliance with ethical standards

Conflict of interest On behalf of all authors, the corresponding author states that there is no conflict of interest.

References

1. Kothari K, Radhakrishnan R, Wereley NM (2012) Advances in gamma titanium aluminides and their manufacturing techniques. Adv Aerosp Sci 55:1–16
2. Kim YW (1989) Intermetallic alloys based on gamma TiAl. JOM 41:24–30
3. Toshimitsu T, Kentaro S, Satoshi K, Satoru K, Masao T (2005) Fabrication of TiAl components by means of hot forging and machining. Intermetallics 13:971–978
4. Appel F, Paul JDH, Oehring M (2011) Gamma titanium aluminide alloys: science and technology. Wiley-VCH, Weinheim
5. Chen G, Peng Y, Zheng G, Qi Z, Wang M, Yu H, Dong C, Liu CT (2016) Polysynthetic twinned TiAl single crystals for high-temperature applications. Nat Mater 15:876–881
6. Li T-R, Liu G-H, Xu M, Fu T-L, Tian Y, Misra RDK, Wang Z-D (2018) Hot deformation behavior and microstructural characteristics of Ti–46Al–8Nb alloy. Acta Metall Sin (English Letters) 31:933–944
7. Uvira JL, Jonas JJ (1968) Hot compression of Armco iron and silicon steel. Trans Metall Soc AIME 242:1619–1626
8. Evans RW, Scharning PJ (2001) Axisymmetric compression test and hot working properties of alloys. Mater Sci Technol 17:995–1004
9. http://ww.ebsd.com/solving-problems-with-ebsd/ebsd-advancement. Accessed 12 Dec 2018
10. Donald S, Kim YW (2007) Sheet rolling and performance evaluation of (β-γ) alloys. In: Ninomi M, Akiyama S, Ikeda M (eds) Ti-2007 science and engineering. The Japan Institute of Metals, Kyoto
11. Appel F (2012) Phase transformations and recrystallization processes during synthesis, processing and service of TiAl alloys. In: Sztwiertnia K (ed) Recrystallization. Intech Open Science, Croatia, pp 225–266
12. Liu B, Liu Y, Li YP, Zhang W, Chiba A (2011) Thermomechanical characterization of β-stabilized Ti–45Al–7Nb–0.4 W–0.15B alloy. Intermetallics 19:1184–1190
13. Zener C, Hollomon JH (1944) Effect of strain rate upon plastic flow of steel. J Appl Phys 15:22–27
14. Sellers CM, McTegart WJ (1966) On the mechanism of hot deformation. Acta Metall 14:1136–1138
15. Prasad YVRK, Gegel HL, Doraivelu SM, Malas JC, Morgan JT, Lark KA, Barker DR (1984) Modeling of dynamic material behavior in hot deformation: forging of Ti-6242. Metall Mater Trans A 15:1883–1892
16. Prasad YVRK, Seshacharyulu T (1998) Modelling of hot deformation for microstructural control. Int Mater Rev 43:243–258
17. Salishchev GA, Senkov ON, Imayev RM, Imayev VM, Shagiev MR, Kuznetsov AV, Appel F, Oehring M, Kaibyshev OA, Froes FH (1999) Processing and deformation behaviour of gamma TiAl alloys with fine grained equiaxed microstructure. Adv Perform Mater 6:107–116
18. Chr Herzig, Przeorski T, Mishin Y (1999) Self-diffusion in γ-TiAl: an experimental study and atomistic calculations. Intermetallics 7:389–404
19. Sprengel W, Oikawa N, Nakajima H (1996) Single-phase interdiffusion in TiAl. Intermetallics 4:185–189
20. Kong F, Chen Y, Zhang D, Zhang S (2012) High temperature deformation behavior of Ti–46Al–2Cr–4Nb–0.2Y alloy. Mater Sci Eng, A 539:107–114
21. Imayev V, Khismatullin T, Imayev R (2010) Microstructure and technological plasticity of cast intermetallic alloys on the basis of γ-TiAl. Phys Met Metallogr 109:402–410
22. Semiatin SL, Chesnutt JC, Austin CM, Seeharaman V (1997) Processing of intermetallic alloys. In: Nathal MV, Darolia R, Liu CT, Martin PL, Miracle DB, Wagner R, Yamaguchi M (eds) Processing of intermetallic alloys (Proceedings of 2nd international symposium on structural intermetallics). The Minerals, Metals and Materials Society, Warrendale, pp 263–276
23. Clemens H, Wallgram W, Kremmer S et al (2008) Design of novel β-solidifying TiAl alloys with adjustable β/B2-phase fraction and excellent hot-workability. Adv Eng Mater 10:707–713
24. Xu XJ, Lin JP, Wang YL, Gao JF (2006) Microstructure and tensile properties of as-cast Ti–45Al–(8–9)Nb–(W, B, Y) alloy. J Alloys Compd 414:131–136
25. Bartels A, Kestler H, Clemens H (2002) Deformation behaviour of differently processed γ-titanium aluminides. Mater Sci Eng, A 329:153–162
26. Whang SH, Hahn YD (1990) Dislocation reaction at 1000°C in L1o type Ti–Al–Nb compound. Scr Metall Mater 24:1679
27. Imayev RM, Imayev VM, Khismatullin T, Oehring M, Appel F (2006) New approaches to designing alloys based on γ-TiAl + α₂-Ti₃Al phases. Phys Met Metallogr 102:105–113
28. Inui H, Kishid K, Misaki M, Kobayashi M, Shirai Y, Yamaguchi M (1995) Temperature dependence of yield stress, tensile elongation and deformation structures in polysynthetically twinned crystals of TiAl. Philos Mag A 7:1609–1631
29. Chang HC, Grant NJ (1956) Mechanism of intercrystalline fracture. Trans AIME 206:544–551
30. Roberts W (1984) Dynamic changes that occur during hot working and their significance regarding microstructural development and hot workability. In: Krauss G (ed) Deformation processing and structure. ASM, Metals Park, pp 109–184
31. Seetharaman V, Semiatin SL (1998) Intergranular fracture of gamma titanium aluminides under hot working conditions. Metall Mater Trans A 29:1991–1999
32. Nobuki M, Hasimoto K, Takahashi J, Sujimoto T (1990) Deformation of cast TiAl intermetallic compound at elevated temperature. Mater Trans, JIM 31:814–819

33. Semiatin SL, Seetharaman V (1997) A criterion for intergranu-lar failure during hot working of a near-gamma titanium alu-minide alloy. Scripta Mater 36:291–297

34. Singh V, Mondal C, Kumar A, Bhattacharjee PP, Ghosal P (2019) High temperature compressive flow behavior and associated microstructure development in a β-stabilized high Nb-contain-ing γ-TiAl based alloy. J Alloys Compd 788:573–585. https://doi.org/10.1016/j.jallcom.2019.02.207

35. Niu HZ, Chen YY, Xiao SL, Kong FT, Zhang CJ (2011) High tem-perature deformation behaviors of Ti–45Al–2Nb–1.5 V–1Mo–Y alloy. Intermetallics 19:1767–1774

36. Jiang H, Zeng S, Zhao A, Ding X, Dong P (2016) Hot deformation behaviour of β phase containing γ-TiAl alloy. Mater Sci Eng, A 661:160–167

37. Zhang H, Xu WC, Shan DB (2009) Hot compression and micro-structural evolution of Ti–43Al–5Nb–0.03Y, alloy. Rare Met Mater Eng 38:1368–1372